Acta Geotechnica (2023) 18:4599–4614
https://doi.org/10.1007/s11440-023-01860-1

RESEARCH PAPER

Role of particle rotation in sheared granular media

Usman Ali[1] · Mamoru Kikumoto[1] · Ying Cui[1] · Matteo Ciantia[2] · Marco Previtali[2]

Received: 9 October 2022 / Accepted: 3 March 2023 / Published online: 20 March 2023

Abstract
When granular assemblies are subject to external loads or displacements, particles interact with each other through contact and may exhibit translations and rotations. From a micromechanical perspective, particle rotations are an essential mechanism influencing the macroscopic behavior of granular materials. In this study, biaxial shearing tests were conducted on assemblies of dual-sized circular particles at different confining pressures. A high-precision image analysis method was developed to extract the particle-level motion of all the particles, including the rotational behavior. Experimental results showed that most of the particles exhibited rotations. Particles within the shear band exhibited more significant rotations and were characterized by low connectivity (number of contacts per particle). In contrast, the particles outside the shear band rotated lesser, only in the beginning stage of shearing. Every rotation in either direction is accompanied by an opposite rotation of almost the same magnitude in the neighboring region, and rotation clusters have been observed. Rotations in both directions are normally distributed within the assembly, and the average particle rotation is zero. The average rotations in both directions evolve symmetrically with major principal strain. Generally, the rotation rate (degrees per incremental strain) is observed to be maximum at the start of the shearing, and gradually it becomes constant toward the end of the shearing. The average value of the absolute cumulative rotation observed for whole particles is 18.6° at the end of shearing, i.e., 20% deviatoric strain. Smaller size particles tend to exhibit 67% higher rotations than bigger particles. Confining pressures have no significant effect on the rotational behavior of circular particles.

Keywords Biaxial shearing · Granular material · Image analysis · Microscopic mechanism · Particle rotation

1 Introduction

The macro-scale behavior of granular assemblies results from mechanical processes at the particle level. Whenever a granular assembly is externally loaded, the particles composing it, in response to such external solicitations, will interact through mechanical contacts and may be displaced from their original position or subject to particle-level damage [21]. Although such microscale responses govern the macroscopic deformation of the granular assembly, microscopic particle rotations did not receive enough attention, and frictional sliding between grains was assumed to control the macroscopic stiffness of granular assemblies [12, 27]. By studying the mechanism controlling fabric reconstruction during the deformation of sand, Oda [22] found that macroscopic deformations occur primarily due to inter-particle sliding and partly due to the rolling of particles. The importance of particle rolling was highlighted by Oda [23] through a series of biaxial tests using cylindrical rods in a pseudo-2D environment. They

✉ Mamoru Kikumoto
kikumoto-mamoru-fc@ynu.ac.jp

Usman Ali
ali-usman-dp@ynu.jp

Ying Cui
sai-ei-mx@ynu.ac.jp

Matteo Ciantia
m.o.ciantia@dundee.ac.uk

Marco Previtali
m.previtali@dundee.ac.uk

[1] Department of Civil Engineering, Yokohama National University, Yokohama, Japan

[2] School of Science and Engineering, University of Dundee, Dundee, Scotland, UK

showed that particle rolling is a major microscopic mechanism that affects granular behavior, especially when interparticle friction is significant. Since then, Image-based experimental techniques have emerged as valuable tools for estimating particle rotation. However, the accuracy of the image analysis to estimate particle kinematics varies depending upon the type of soil, image acquisition process, and method adopted. Digital image correlation (DIC) is a widely used technique in experimental investigations of grain kinematics by comparing different images [11, 24, 29]. DIC can be classified based on the dimensions of the images. For example, surface-DIC is based on 2D images, while Volumetric-DIC or digital volumetric correlation (DVC) are based on 3D images [26].

Misra [19] studied the deformation patterns of around 600 multi-sized circular aluminum and plastic rods in a biaxial test with a quasi-static loading process and mixed boundary conditions to check the particle rotations. They found out the average particle rotation within the sample was close to zero, as the clockwise rotation of a particle was associated with counterclockwise rotation in the surrounding particles and vice versa. Calvetti [4] investigated the micromechanics of multi-sized circular wooden rods using special 2D shear apparatus. The behavior of rods was analyzed under complex loading conditions involving loading–unloading cycles and rotations of principal axes. Out of 750 rods used in the testing, only 300 in the central part of the shear box were traced. Pictures were taken during the loading to characterize the micromechanical variables and their evolution. They observed that particle rotations were an important micromechanical parameter in granular deformations. Chen [6] developed an algorithm to estimate the rotations of particles from 2D images; however, it required very high-quality images of a particular type of surface-treated material. Despite being very challenging, measuring particle rotation in 3D experiments such as triaxial compression using X-ray Scanning images has greatly helped increase our knowledge of natural sand. Lenior [17] and Hall [11] used DVC to correlate 3D images acquired by X-ray microtomography to study localized deformations and grain kinematics. Ando [1] studied micromechanics of granular assemblies using X-ray tomography to obtain 3D images of the triaxial sand specimens. A 3D image analysis technique was used to digitally correlate the 3D images to estimate individual grain kinematics. Results showed that grain rotations were a crucial mechanism in granular materials. For the acquisition of 3D images, the tests were performed in situ in an X-ray scanner, allowing the sand specimens to be scanned under load. Such a scanning process requires a pause in loading of 12 to 15 min to keep the axial strain constant during scanning to obtain high-resolution images. This unavoidable aspect causes axial load relaxation, and the samples undergo creep and micromechanical developments that we cannot observe.

Since the development of the discrete element method (DEM) [10] and following the early experiments such as those by Oda [23] and Misra [19], the use of micromechanical modeling to investigate the fabric evolution of sheared granular assemblies has helped to shed light to many unanswered questions. Bardet [3] studied the structure of shear bands by simulating idealized granular media. They confirmed that particle rotations concentrate inside shear bands. The concentration of particle rotations inside the shear bands was also observed in other DEM studies [2, 14, 18, 26]. Bardet [2] performed simulations of the biaxial test in which rotations were numerically suppressed and concluded that the shear strengths of granular material were significantly affected by particle rotations. Kuhn [15] performed DEM simulations of biaxial shearing tests with circular disks. Most rapid rotations were found to be occurring within dominant deformation zones. The rotations ease sliding between most of the particles and transfer the sliding to a few contacts where the frictional slipping was intense. Kuhn [16] simulated the biaxial test with multi-sized circular particles in DEM. The whole assembly was partitioned into polygonal regions to discuss two mesoscale phenomena, rotating clusters and rotating chains. They observed that grains within a rigid part usually rotate in the same direction. Most high-spin particles were in chain-like patterns oblique to principal stress directions, usually located within intensely deformed regions. The net effect of particle rotation reduces the stiffness and strength of granular materials. Additionally, when particle rotations are artificially restricted in simulations, the stiffness and strength of the assembly increase, and the localized failure patterns assume different shapes [2]. Following the 3D experimental investigations mentioned above, Rorato [26] used 3D DEM to study the micromechanics of sand, especially the particle rotations inside and outside strain localized zones.

Although particle rotation has been recognized as an essential microscopic mechanism affecting granular behavior, accurate 2D particle kinematics observed in the laboratory are still very limited and have been obtained only on small samples of a few hundred particles. Contrary to 3D experiments, 2D experiments do not require a pause in loading for scanning the specimen. Instead, a high-resolution digital camera can take pictures during loading without allowing any load relaxation. Moreover, over the last few decades, the DEM has become a powerful tool for investigating the micro-deformation mechanisms in granular systems because, in DEM, the particle-level information can be observed easily relative to laboratory experiments [33]. However, the DEM requires a validation/calibration process. Validation of the DEM model is

usually done by matching with the macroscopic stress–strain experimental data from an elementary test [20, 31]. However, such a macroscopic validation process cannot confirm the rationality of particle-level mechanisms. Hence, a detailed validation process should also consider the particle-level phenomenon to increase the reliability of virtual experiments. Furthermore, the most common particle shape used in DEM is either circular disks in 2D or spheres in 3D simulations for efficient contact detections and easy computations [25]. The shape of actual soil and other particles is far from the ideal shapes commonly used in DEM [13]. Therefore, when comparing the macroscopic stress–strain data of natural soils with the DEM results from ideal shapes, the particle-level mechanism can differ significantly even though the macroscopic stress–strain data shows a good match. This is because the actual particle shape in a granular system affects the particle-level interactions [7]. Consequently, when using ideal shapes in modeling granular systems, the validation process should ideally compare the numerical results with data from an elementary test conducted with similar ideal shape samples. This study provides a complete data set of circular disks, including macroscopic stress–strain response and microscopic particle motions, such as particle-level rotation and fabric evolution. The data set enables substantial validation of particle-based simulation models such as DEM.

In this study, the biaxial shearing tests are conducted on assemblies of bi-disperse aluminum circular rods using 2674 particles. A detailed image analysis method is designed to capture the kinematics of circular particles. The surfaces of all the particles were treated by pasting special kinds of stickers, and high-quality photos were captured during the experiment. The Multiscale Analysis for the Granular Image Correlation algorithm developed by [6] is then used to identify and track particle motions, including rotations under three different confining pressures. Particle scale information is then used to advance our understanding of sheared granular systems by looking at individual and cluster behavior and tracking the fabric evolution of the sample.

2 Outline of biaxial tests

2.1 Biaxial apparatus

A schematic view of the apparatus is shown in Fig. 1. The dimensions of the specimen box are 350 mm × 350 mm at the initial state, and the depth of the rigid walls is 50 mm. The specimen boundaries are surrounded by rigid aluminum walls, wherein rotations of the walls is prevented completely. The bottom wall is fixed, and the top and side walls are only allowed to move in the direction normal to their boundaries. Since the front and back sides of the specimen are open, the aluminum rods used as the two-dimensional granular model are kept under a plane strain condition.

Load and displacement in both vertical and lateral directions are measured throughout the test. Either load or displacement in the vertical and lateral directions, respectively, can be controlled in this apparatus, and the control can be arbitrarily switched. The load is controlled with the pneumatic cylinders, and the displacement is applied by the screw jacks. The vertical displacement of the top wall is obtained by averaging the displacements of the right and left ends of the wall measured by two displacement transducers. The relative lateral displacement of the side walls is measured by fixing a displacement transducer on the left wall and measuring the displacement of the right wall. Major and minor principal strains are obtained by dividing vertical and lateral displacements by the initial height and width of the specimen, respectively. In the horizontal direction, when the pneumatic cylinder II pushes on the right wall, the reaction force of the cylinder acts on the rigid frame with the left wall. As a result, the same stress acts on the left and right walls. The vertical load is obtained by averaging the measurements of two load cells installed at the top and bottom walls, and the lateral load was measured by a load cell installed at the right wall. The maximum and minimum principal stresses are determined by dividing the vertical and lateral loads by the current varying cross-sectional area of the specimen orthogonal to the corresponding direction. The cross-sectional area is continuously updated using the measured vertical and lateral displacements; a data logger connected to the PC collects the displacements and loads. During the shearing process, the PC automatically measures the change in cross-sectional area and controls the minor principal stress to be constant by sending an appropriate pressure to the pneumatic cylinder with an electro-pneumatic regulator and DA board.

For load-controlled loading, the major and minor principal stresses are continuously monitored by the PC and controlled by sending the target air pressures to the pneumatic cylinders I and II, respectively. The air pressures sent to pneumatic cylinders are controlled by the PC by sending prescribed voltage signals to electro-pneumatic regulators via a digital-analog board. During the isotropic compression process, the minor principal stress is automatically controlled to be the same as the major principal stress. During the shearing stage, a constant major principal strain rate is applied by the screw jack while the minor principal stress is kept constant.

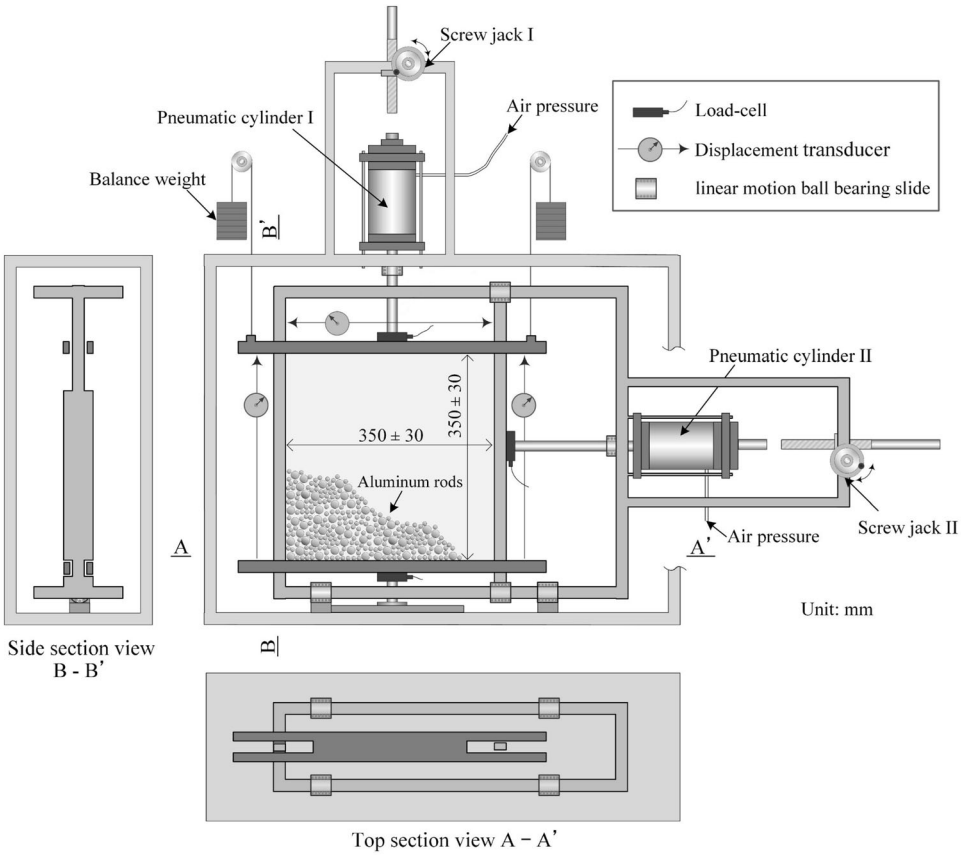

Fig. 1 A schematic plan of the biaxial test apparatus

2.2 Test procedure and testing patterns

A series of consolidated-drained (CD) biaxial tests are carried out. The aluminum rods are manually placed layer by layer in the specimen box with an initial void ratio of 0.215. As the self-weight of aluminum rods acts on the bottom wall, the load cell installed at the bottom wall records the applied load from the top wall and the weight of the rods. Therefore, the average of top and bottom cells is used as vertical load. The specimen is compressed isotropically by increasing major and minor principal stresses simultaneously until the desired confining pressure is reached. The sample is then sheared by applying a constant major principal strain rate, i.e., 0.014% per second (0.05 mm/second), keeping confining stress (minor principal stress) constant. In this study, biaxial tests are conducted at three different confining pressures (σ_3 = 19.6, 39.2, and 58.8 kPa). The repeatability of the tests was confirmed by performing multiple tests under the same testing pattern.

2.3 Granular material

The granular material used in the experiment comprises dual-size aluminum rods of 10 mm and 6 mm diameters. The length of all rods is 50 mm, equal to the depth of the biaxial sample box. The mixing ratio of big to small particles is 2:3 by weight. Aluminum rod material is widely accepted for studying the mechanical behavior of granular materials under plane strain conditions [28]. The density of the aluminum rods is 2830 kg/m^3, and the specific weight of the specimen is around 22.5 kN/m^3. Figure 2 shows the materials used. The aluminum-aluminum friction coefficient under smooth and dry conditions is observed to be 0.2 by conducting direct shear tests on aluminum disks.

Surface treatment of the aluminum bars is required before testing to detect the microscopic motion and rotation of the particles. For that, circular black stickers are glued to the end of each rod. Two dots of red and green colors on the black circular background enable the identification of particle rotation. The size of stickers is smaller than the actual sizes of particles for easy and firm placement, i.e.,

8.3 mm for 10 mm particles and 5 mm for 6 mm particles. Therefore, the ratio of the actual particle and sticker sizes is constant. Surface treatment is seen in Fig. 2.

2.4 Image acquisition process

The image acquisition arrangements are shown in Fig. 3. The movements of the particles are grasped by taking digital photos of the specimen and analyzing them by image analysis. Digital photos of 24.35 megapixels (6016 × 4000) are taken during the shearing test by a digital camera positioned at around 600 mm on the front side of the test chamber. Surrounding lighting is arranged to obtain adequate uniform illumination. Moreover, the backside of the test chamber is also illuminated to increase the visibility of the voids. The diameter of circular stickers on small particles corresponds to approximately 50 pixels on a digital image, while that on big particles corresponds to approximately 83 pixels. The acquired images are stored in JPEG-colored image format.

3 Image analysis methodology

3.1 Image processing

Image processing aims to enhance the visibility of the particles in all the photos by adjusting the intensity and applying other image adjustment techniques for easy identification. The open-source software ImageJ/Fiji is used for image processing. The steps used in processing involve grayscale conversion and intensity adjustment.

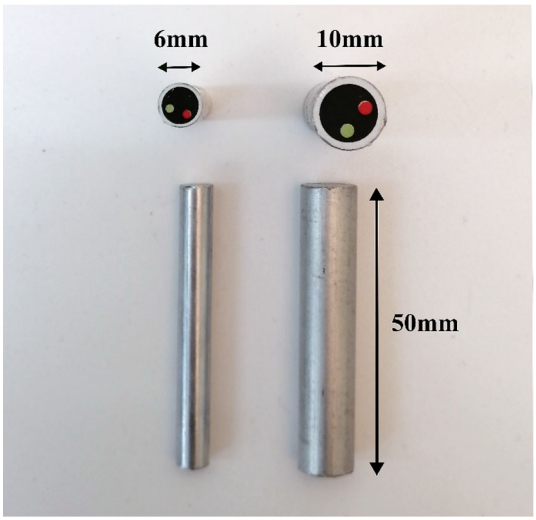

Fig. 2 Surface-treated aluminum bars used for biaxial testing

3.2 Particle identification

Particles were identified using MATLAB's built-in function "imfindcircles" with sensitivity and threshold values of 0.9 and 0.1, respectively. Black surface treatment confirms the object's polarity to be dark over a bright background. Centroid coordinates of all the stickers glued on particle cross sections are identified successfully due to the surface treatment and high-quality images. The success rate of the identification process was ∼ 100%. Figure 4 shows the image of particles and the results of size-wise particle identification.

3.3 Particle tracking

The tracking algorithm [9] detects particle translation. The trajectories include only the translational movement of the particles, not their rotation. The algorithm requires a user-defined search radius and searches for their subsequent locations in the next image. Once a user-defined search radius is assigned, there are three possibilities: unique match, multiple new locations, and particle loss. A unique match is when the algorithms detect only one new location within the assigned search radius in the next image. A higher value of search radius may lead to the detection of multiple new locations. If this happens, the algorithms will assume the closest new position is the actual new position of the particle. It could be possible that no new location was found within the search radius; this is rare but true in case of wrong particle identification or if the search radius assigned is very small.

Ideally, the search radius should be no larger than the smallest particle that needs to be tracked, which is 50 pixels (small sticker diameter resolution) in this study. If the search radius is larger than the small sticker size, the algorithm may incorrectly detect the center of another surrounding particle in the next image. Therefore, to successfully identify the same particle between two consecutive images, it is preferred that the movement of the particle between frames is limited to less than the size of the particle. In this study, the interval between two consecutive images was determined to be 25 to 30 s, considering the applied major principal strain rate. This time interval between frames ensured that small particles did not move beyond their size and that the same particle could be reliably identified during the particle tracking process. The tracking process is repeated so that the centroid locations of each particle are uniquely identified in all images. Further details about the tracking process can be found in [6, 9]. Figure 5 shows the trajectories of particles after digital image correlation analysis.

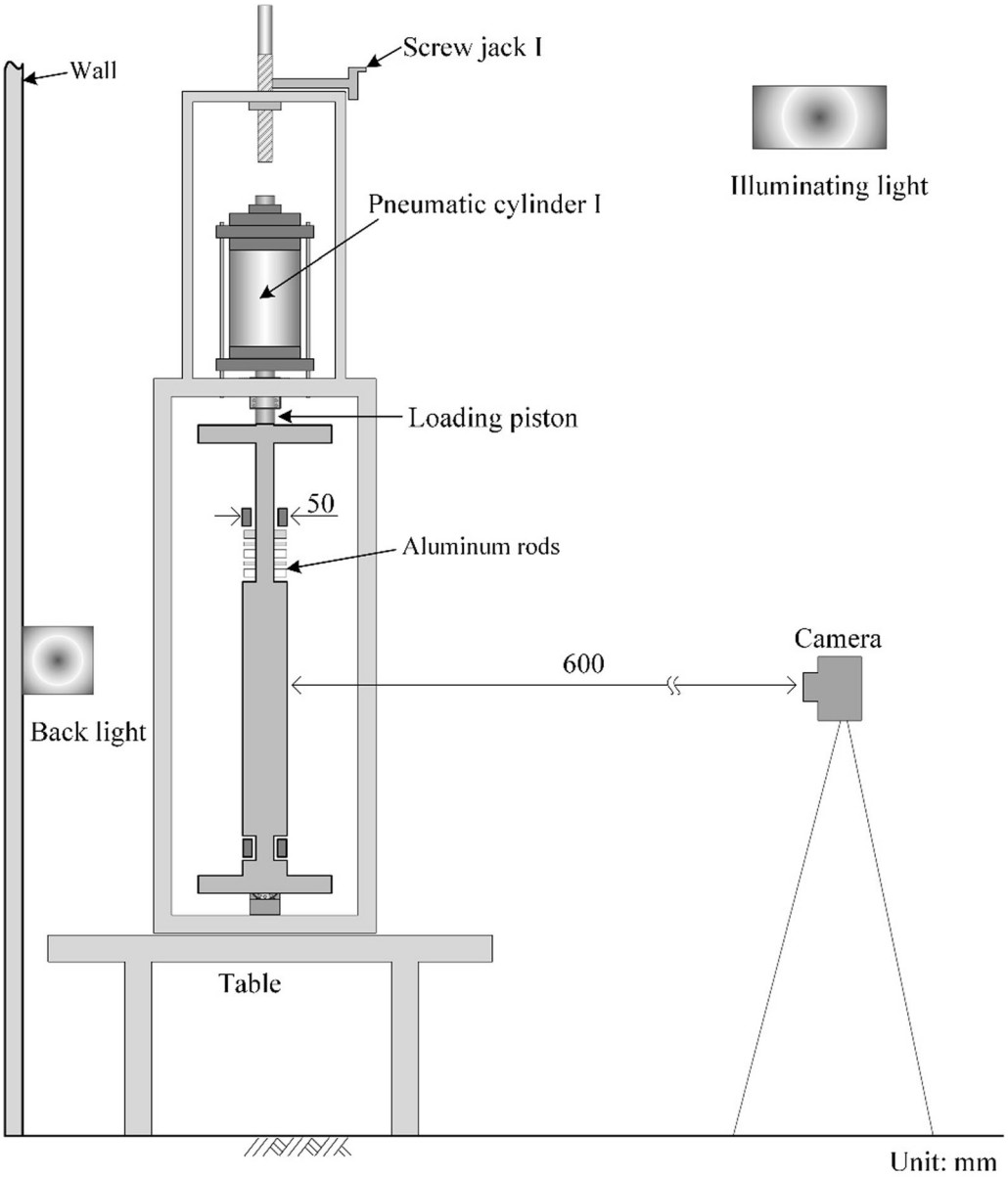

Fig. 3 Schematic view of image acquisition arrangements in the laboratory

3.4 Particle rotation

Rotation detection algorithms used in this study were originally developed by Chen [6]. The rotation of particles during the biaxial test can be estimated by the correlation between two consecutive images taken during the test. Rotation algorithms require an input of particle tracking results to identify the position of the same particle in the next photos and the grayscale images of particles. For each of the two consecutive photographs taken during the experiment, the center position of the circular black target affixed to each particle is identified using an image analysis algorithm, and the incremental displacement vector of the particle is obtained by comparing the location of the target in the two photos. Next, the center positions of the smaller green and red circular targets placed inside the black circular target in the two photographs are identified and used to obtain the incremental rotation of the particle. The same process is repeated for all photographs taken throughout

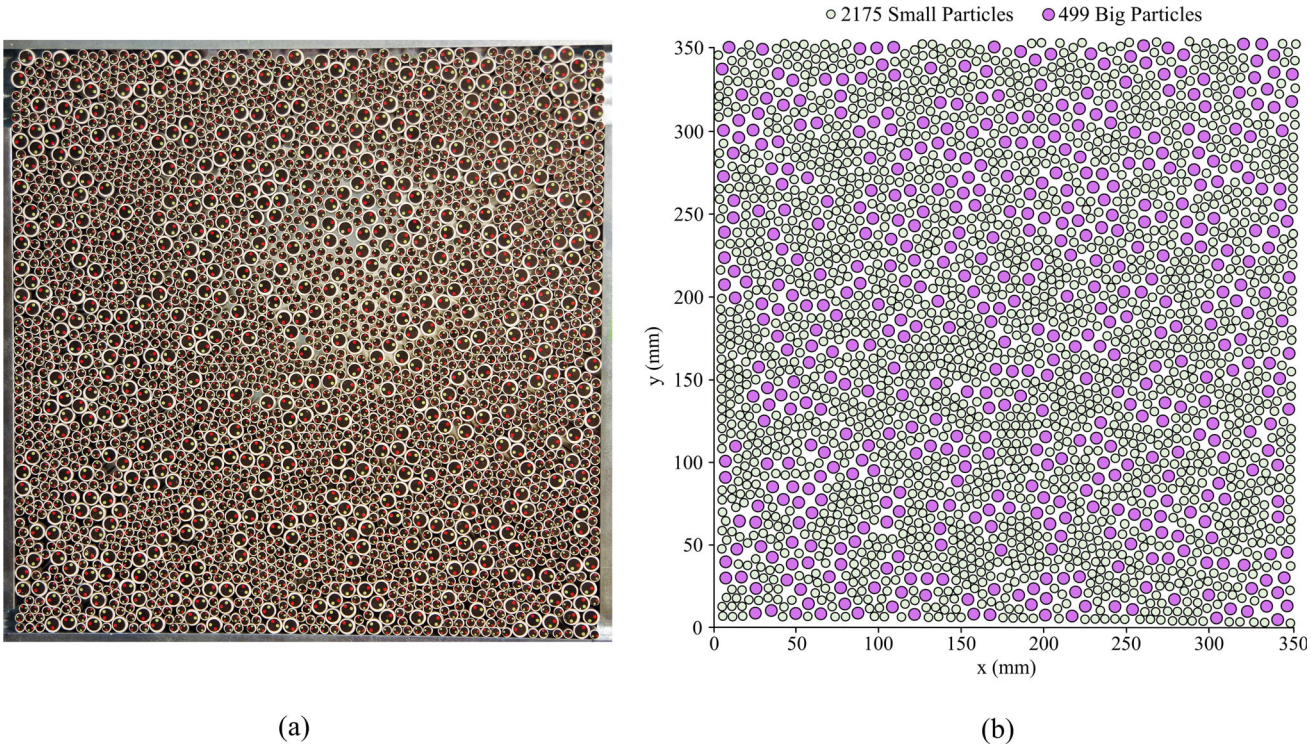

Fig. 4 Particle identification **a** Photo of the particles in biaxial chamber, and **b** particle identified size-wise

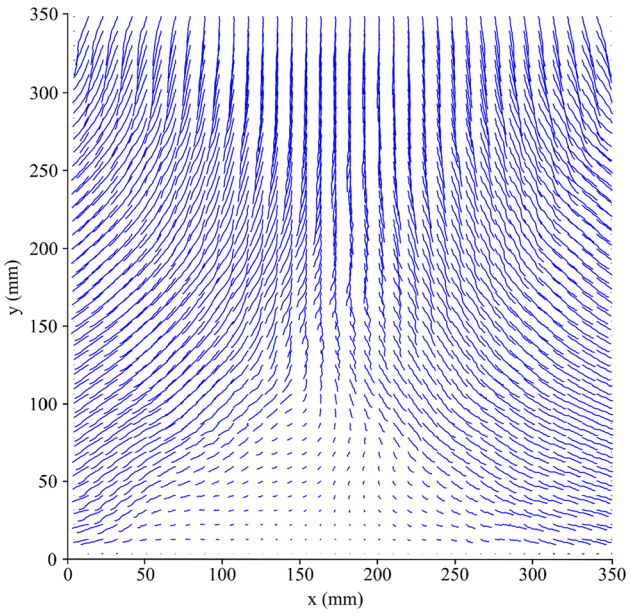

Fig. 5 Particle trajectories movements during the shearing test

the experiment to obtain the incremental displacement vectors and incremental rotations for all particles and then sum them up to evaluate the cumulative displacement and cumulative rotation of the particles, respectively. A similar particle may rotate either clockwise or counterclockwise during the test, but the net rotation is the final angular displacement from the original orientation. The clockwise rotations are measured with a negative sign and counter-clockwise with a positive. The net rotation of a single particle is obtained by the summation of the rotation of all photo pairs. The method to estimate the rotation uses 8-bit grayscale images and is called Intensity-based image registration. Further details about rotation algorithms can be found in [6].

3.5 Validation of rotation algorithms

To evaluate the accuracy of the intensity-based image registration algorithms, 30 surface-treated particles, including 7 big and 23 small particles, are placed in a biaxial testing type arrangement. The image is captured as shown in Fig. 6a and converted into a grayscale image using ImageJ. Then, as the incremental absolute rotation observed between two consecutive photographs taken during the biaxial test was approximately 2° to 3°, the algorithm for analyzing particle rotation was validated using an image of aluminum rods and a processed image of a 2° clockwise rotation to it. The process explained above is applied to the same pair of these images (original and 2° rotated). After performing the particle identification and tracking process, the results of the tracking process and pair

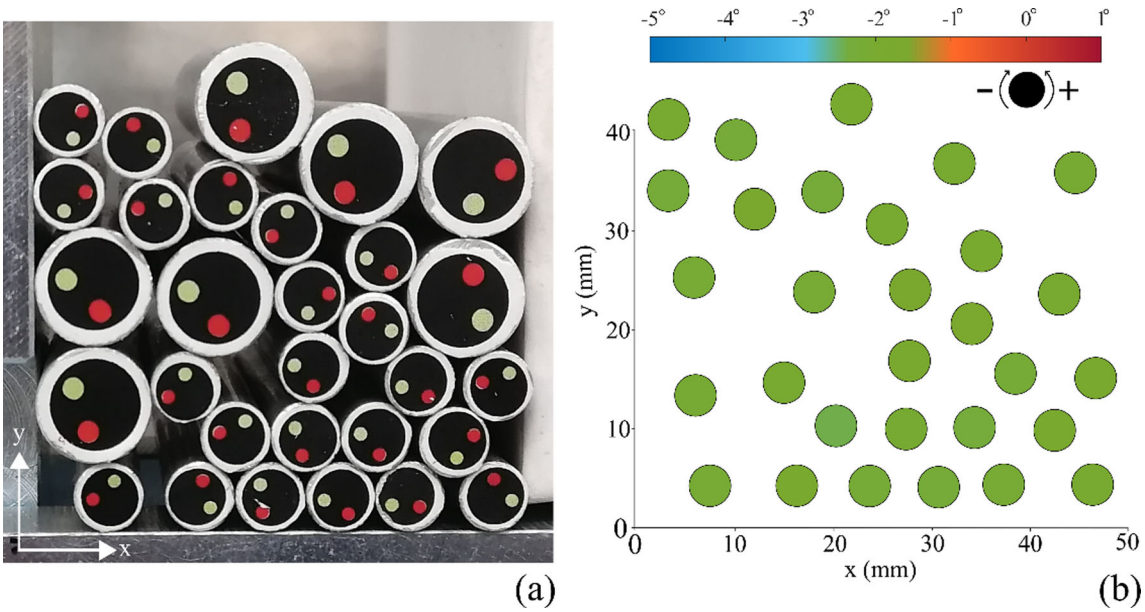

Fig. 6 Validation of rotation detection algorithm **a** 30 selected particles for the validation **b** estimated particle rotations obtained from the original and artificially rotated images (negative sign indicates clockwise rotation)

grayscale images are used as input to the rotation process. Figure 6b shows the spatial distribution of the results of the rotation analysis. The average particle rotation is 2.05° for all particles, with an average accuracy of about 97% and a standard deviation of 0.18°.

4 Results and discussion

4.1 Biaxial test results

Figure 7 shows the stress–strain relationship and volumetric behavior of aluminum rods. σ_1 and σ_3 are the major and minor principal stresses applied from vertical and lateral directions, respectively. Similarly, ε_1 and ε_3 are the major and minor principal strains exhibited in vertical and lateral directions, respectively. Deviatoric stress (σ_s) is the difference between major and minor principal stresses, σ_1–σ_3. Volumetric strain (ε_n) is the sum of major and minor principal strains ($\varepsilon_1 + \varepsilon_3$), while deviatoric strain (ε_s) is their difference (ε_1–ε_3). It can be seen that both stiffness and strength increase with increasing confining pressure (σ_3), showing the typical behavior of frictional materials. The sample compressed slightly at the initial shearing stage, and the specimen expanded in volume afterward, resulting in positive dilatancy. The macroscopic stress–strain behavior of the aluminum rods corresponds to that of loose to medium-dense sand.

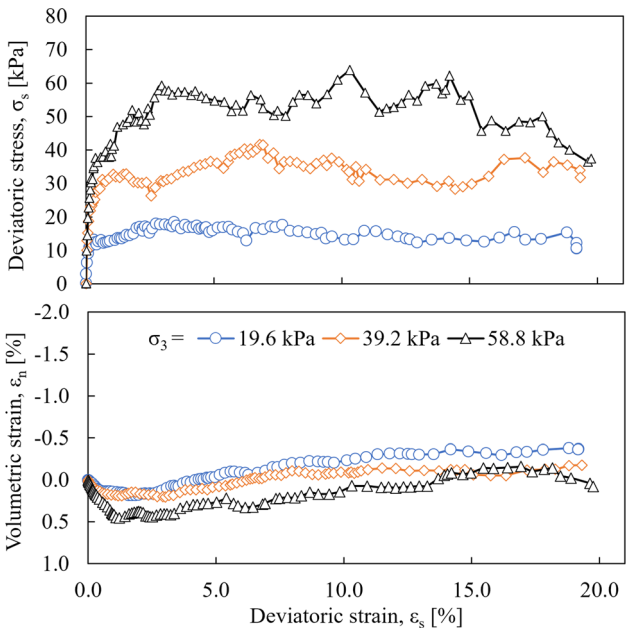

Fig. 7 Stress–strain relationship and volumetric behavior of aluminum rods under different confining pressures

4.2 Rotation of particles

The rotation angle of each particle is estimated by the "Intensity-based image registration method." The success rate of rotation estimation is more than 95% which means out of around 2674 circular particles, rotation of more than 2550 particles is identified.

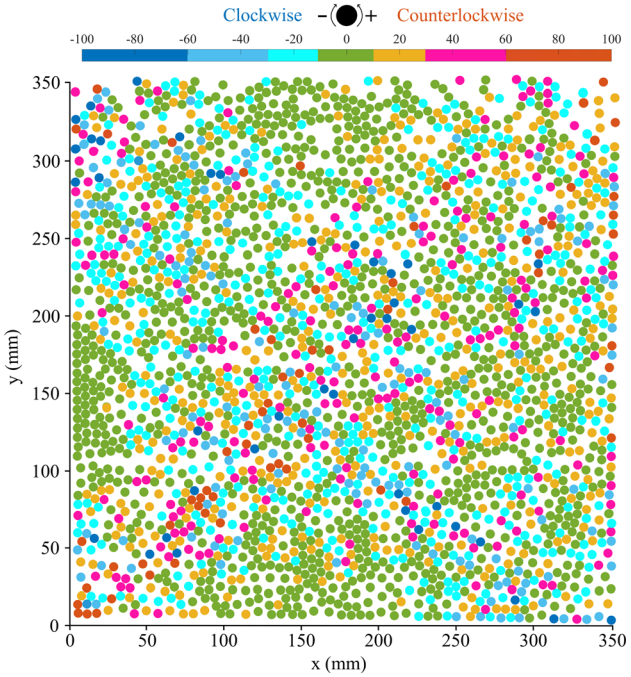

Fig. 8 Cumulative particle rotation in degrees plotted for the biaxial test at 20% deviatoric strain (σ_3 = 39.2 kPa) (negative and positive sign indicates clockwise and counterclockwise rotations)

Figure 8 shows the spatial distribution of cumulative rotations at 20% deviatoric strain in the biaxial chamber for the test conducted under confining pressure σ_3 = 39.2 kPa. The negative sign indicates clockwise rotation, and the positive indicates counterclockwise rotation. Many particles (around 44% of the total) show a cumulative rotation between −10° and 10° (indicated by the green color). However, particles along the diagonals of the biaxial chamber tend to exhibit significant rotations (indicated by blue and red color groups). Blue and red colors indicate clockwise and counterclockwise rotations, respectively.

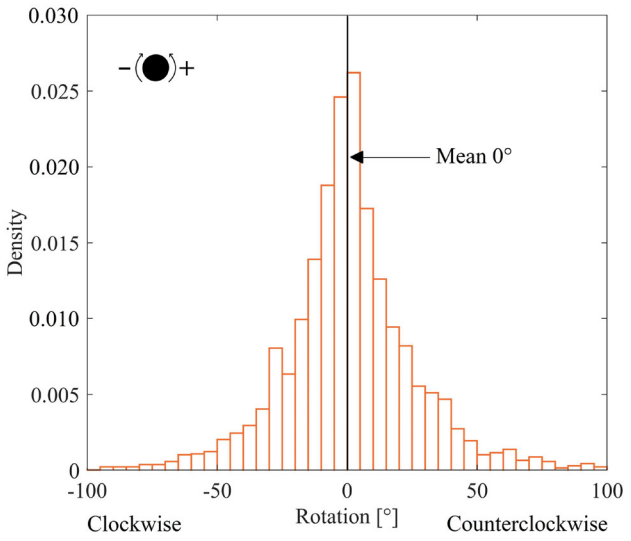

Fig. 9 Cumulative rotation density distribution at 20% deviatoric strain (σ_3 = 39.2 kPa)

Figure 9 shows the density histogram of the cumulative particle rotations. Rotational data is symmetrically distributed around the mean, close to 0 degrees. The normal distribution of particle rotations within the sample was also observed by [19, 23, 26]. The number of particles exhibited clockwise rotations is almost equal to the number of particles rotating counterclockwise. Clockwise rotation is usually accompanied by a counterclockwise rotation of a neighboring particle. It is seen in Fig. 8 that blue markers are usually surrounded by some red or vice versa. In some cases, a group of neighboring particles exhibits rotation in the same direction forming a rotation cluster. In such a situation, an opposite rotating cluster can be observed in neighboring regions. The formation of rotation clusters within biaxial assemblies was also observed by Kuhn [16]. The average cumulative clockwise and counterclockwise rotations at 20% deviatoric strain are 18.2° and 19.0°, respectively. Average cumulative rotations observed in both directions are almost equal, which results in a net rotation within the assembly of nearly zero. Furthermore, the final absolute average cumulative rotation observed for all the particles in the assembly is 18.6°.

4.2.1 Shear band identification

In this study, rigid boundaries are used in the biaxial test, which affects the formation of the shear band. Figure 10 shows the evolution of the cumulative shear strains calculated from displacement fields obtained through conventional DIC analysis using finite strain theory [24]. The mesh size used in DIC analysis for calculating shear strain is around the size of the big particles. At small strains, thin shear strain localization can be seen, especially in the areas along the diagonals of the biaxial box. Kuhn [15] also observed such thin intensely deformed zones which they called microbands in their DEM simulations using periodic boundaries. They further reported that, unlike shear bands, the microbands were neither static nor persistent, they would emerge, move, and disappear. However, as the specimen is sheared with rigid boundaries, a further shear strain localization can be seen along the diagonals with an increase in deviatoric strain, confirming the formation of shear bands. At 8.5% major principal strain, shear strain localization can be seen clearly. This can be concluded that due to rigid boundary conditions, shear localization can be observed along the diagonals of the biaxial chamber.

In shear bands, the constraints on the microscopic behavior of particles are very different [26]. Therefore, particles belonging to the shear zone were identified based on the magnitude of the shear strain. For this, deviatoric

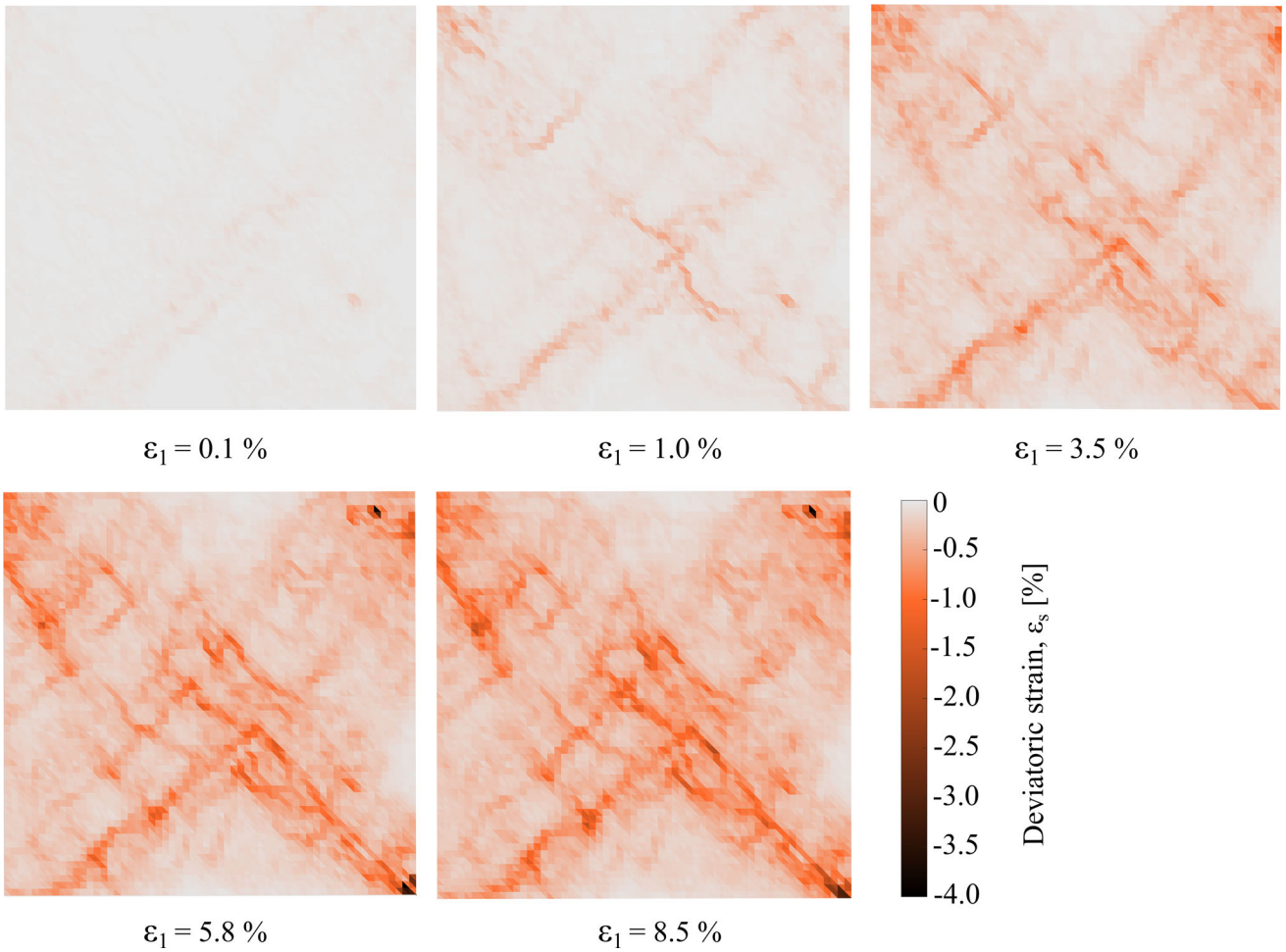

Fig. 10 Cumulative shear strain map from DIC analysis using finite strain theory (σ_3 = 39.2 kPa)

strain is assigned to each particle using a procedure developed for post-processing discrete element results [5]. In this procedure, a Voronoi cell having vertices at the mass centers of the particles (the centers of black stickers pasted on each particle) is identified using a regular Delaunay triangulation available within YADE [30]. Thus, the particle positions in the photos taken at two instants toward the end of shearing (at the major principal strain of 8% and 9%) were identified using the particle identification technique described above. Displacements of neighboring particles were then used to compute a strain tensor for the triangular element. Finally, the deviatoric strain was assigned back to each particle by averaging the deviatoric strain of the adjoining triangular elements, and a threshold deviatoric strain of 5% was applied to identify particles inside the shear band.

The results of the shear band identification procedure are shown in Fig. 11, in which the black particles are identified to be inside the shear band. The two X-shape zones identified correspond closely to those apparent in rotation distribution plots (Fig. 8) and DIC analysis (Fig. 10). The

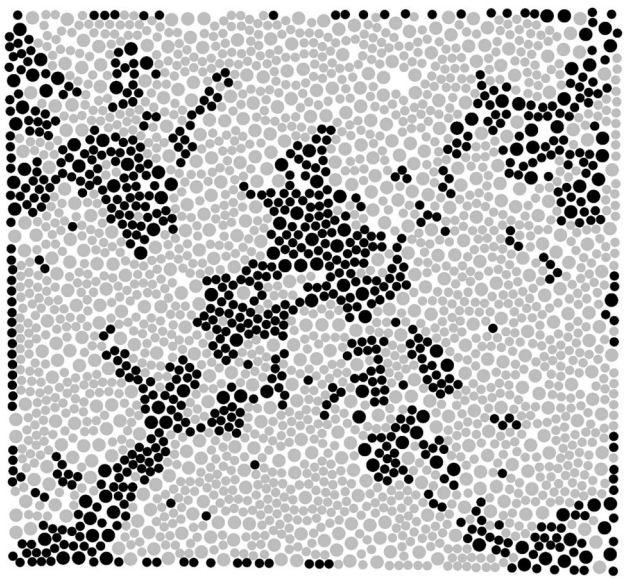

Fig. 11 Particles inside of the shear band at 20% deviatoric strain (black color; σ_3 = 39.2 kPa)

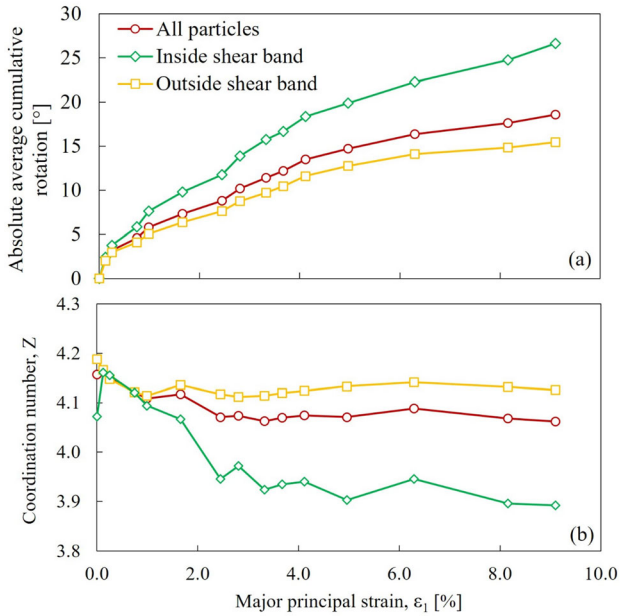

Fig. 12 **a** History of absolute average cumulative rotation inside, outside the shear band, and for complete assembly **b** Coordination number evolution inside, outside the shear band, and for complete assembly (σ_3 = 39.2 kPa)

same procedure was used to determine the shear band by Rorato [26]. After shear band identification, particle rotation and coordination number history can be tracked inside and outside the shear band.

Figure 12a shows the histories of absolute average cumulative rotations for particles inside and outside the shear bands and for all particles. The slope of the curve in Fig. 12a is steeper at the start of the test, which signifies that rotations develop very quickly at the beginning. As the deformations progress, it becomes flatter. The rotations observed inside and outside the shear band show good agreement with the past experimental works [2, 4, 14, 18, 26]. It is seen that the mean cumulative particle rotations inside the shear zone increased significantly from the beginning of shearing and continued to increase even when the cumulative major principal strain exceeded 9.0%. On the other hand, the average cumulative rotations of particles outside the shear zone also increased monotonically, and the increase was larger in the early stage of shearing up to an axial strain of around 4.0%, but the mean absolute rotation was about 40% smaller than that inside the shear zone.

4.2.2 Evolution of coordination number

The coordination number (Z), defined as the average number of contacts per particle (or average connectivity), has been identified as a key microstructural variable of granular systems [8, 32]. Thanks to the accurate and high-resolution image analysis, variations in the coordination number were detected to describe the fabric evolution of the granular system. The size of the black sticker on each particle is slightly smaller than the size of the particle. Therefore, to determine contact between particles, after identifying the outline of the black sticker, its diameter was enlarged by 6.5% to determine contact.

Figure 12b shows the evolution of Z as the major principal strain increases. At the start of the shearing process, Z increases as new contacts are generated in the compression phase, but as the specimen dilates, the Z decreases. Z decreases significantly inside the shear band zones, where higher particle rotations are also measured. This suggests that particle rotation and Z are strongly correlated and that it is easier for the particles to rotate if they have low connectivity.

4.2.3 Evolution of particle rotation with shearing

Figure 13 shows the evolution of cumulative rotation distribution with major principal strain. At the start of the shearing, most particles exhibit no rotation. The histogram of 0.1% major principal strain indicates that only a few particles encounter some rotation, while most particles show no significant rotation. As the major principal strain increases, particles exhibit more rotation, and distribution becomes flatter and broader, indicating that rotation in the assembly grows as the maximum principal strain grows. However, the plots at different major principal strain values are symmetrically distributed around the mean.

Figure 14 shows the increase in average cumulative clockwise and counterclockwise rotation observed for all

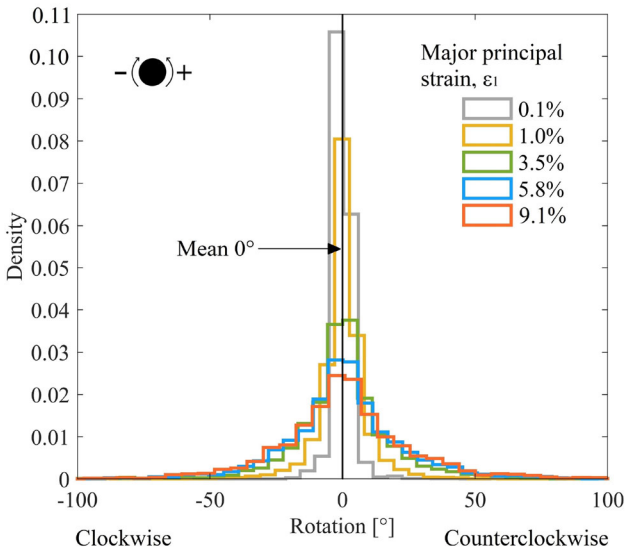

Fig. 13 Cumulative rotation density distribution evolution with major principal strain (ε_1) for complete assembly

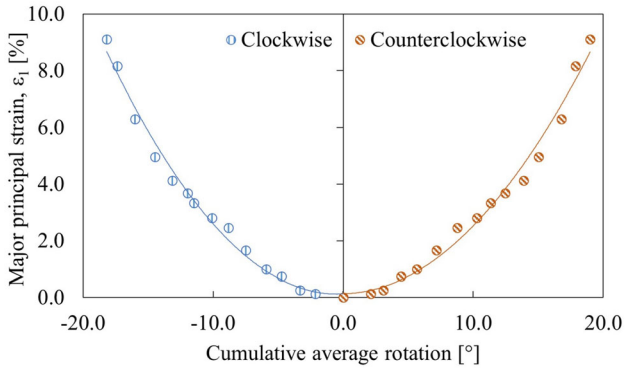

Fig. 14 Cumulative average clockwise and counterclockwise rotation growth with major principal strain (ε_1)

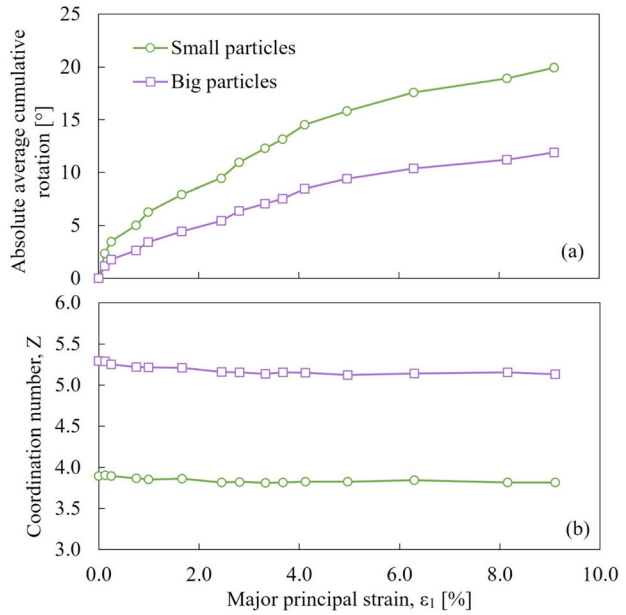

Fig. 15 **a** History of absolute average cumulative rotation for big and small particles **b** Coordination number evolution for big and small particles (σ_3 = 39.2 kPa)

the particles in the assembly with major principal strain. It can be seen that as the major principal strain increases, rotations increase in both directions simultaneously. The relationship between average cumulative rotation in either direction and major principal strain can be nicely explained by a linear polynomial regression function as indicated by thin solid lines. For example, at 1.0% and 3.5% major principal strain, the average clockwise rotation is 5.9° and 11.9°, while at the same instants, the average counterclockwise rotation is 5.8° and 12.2°, respectively. The simultaneous growth of rotation in both clockwise and counterclockwise directions verifies that any rotation in either direction is accompanied by almost the same rotation in the opposite direction throughout the test resulting in

Table 1 Average absolute cumulative rotations observed for small, big particles and complete assembly at around 20% deviatoric strain (σ_3 = 39.2 kPa)

Description	Rotation (°)		
	Small particles	Big particles	Complete assembly
Clockwise	19.6	11.0	18.2
Counterclockwise	20.2	12.8	19.0
Absolute average	19.9	11.9	18.6

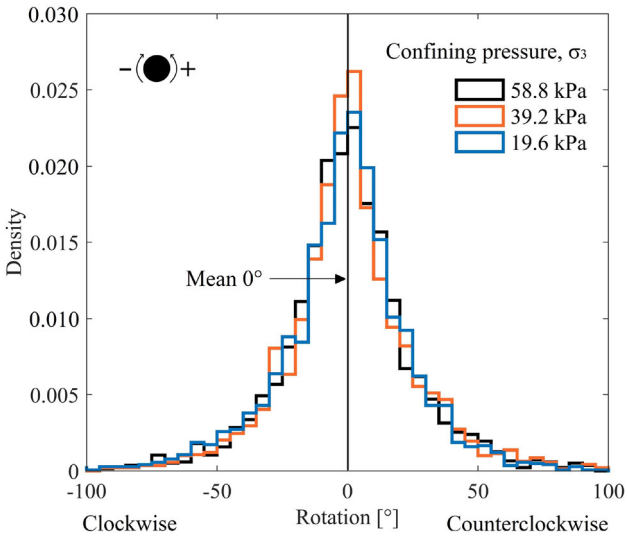

Fig. 16 Cumulative rotation density distribution under different confining pressures at around 20% deviatoric strain

zero average particle rotation. Here it is interesting to note that the average particle rotation keeps close to zero in the tests where the principal strain axes are fixed (walls were not allowed to rotate and the specimen's rigid rotation is fixed). Likewise, Calvetti [4] reported that, in compression and shear tests wherein the principal axes were fixed, the average value of particle rotation was close to the rigid rotation of the specimen. However, the relation between average particle rotation and specimen rigid rotation does not hold in the tests wherein the continuous rotation of principal axes was performed.

4.2.4 Particle size effect on rotation magnitude

Two sizes of circular particles are used in biaxial testing, i.e., 10 mm and 6 mm diameters mixed at a 2:3 mixing ratio by weight. Among 2674 particles, 499 are big and 2175 are small particles. The rotation of small and big particles is analyzed to investigate the effect of particle size. A particle's size tends to affect the rotation

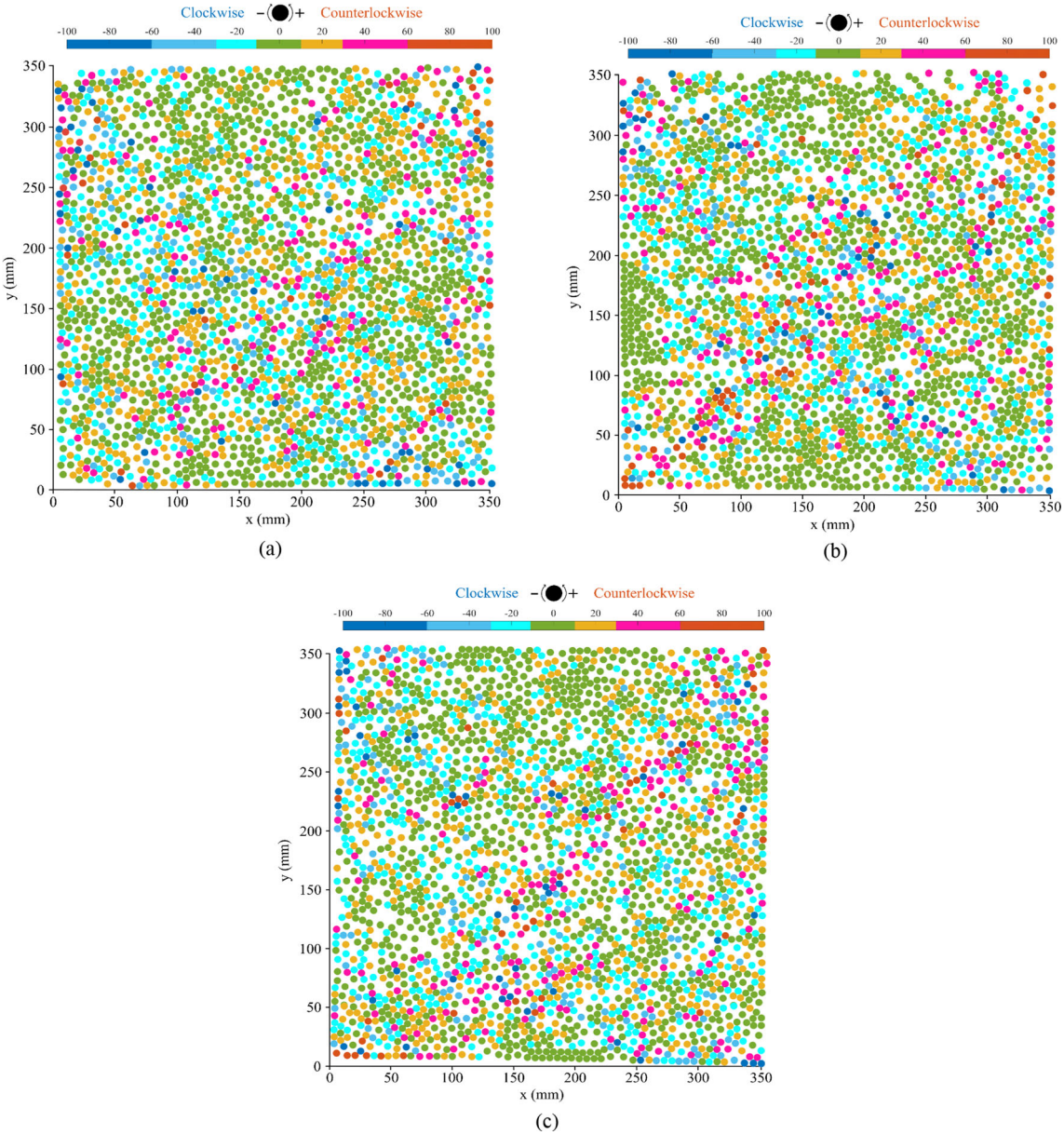

Fig. 17 Spatial distribution of cumulative rotations at around 20% deviatoric strain observed at different confining pressures **a** 19.6 kPa, **b** 39.2 kPa (identical to Fig. 8), and **c** 58.8 kPa

Table 2 Average cumulative rotations observed under different confining pressures at 20% deviatoric strain

Description	Rotation (°)		
	19.6 kPa	39.2 kPa	58.8 kPa
Clockwise	19.71	18.18	18.28
Counterclockwise	17.41	18.99	18.71
Absolute average	18.56	18.59	18.54

magnitude, so smaller particles exhibit higher rotation magnitudes. Figure 15a shows the comparison of observed cumulative rotation for both sizes, wherein it can be seen that as the shearing begins, the bigger particles exhibit lesser rotations. At the end of shearing, the absolute average rotation is 19.9° and 11.9° for small and big particles, respectively. On average, each small particle exhibits around 67% higher rotation magnitude. Figure 15b shows the evolution of the average coordination number for both sizes. It is observed that bigger particles tend to maintain a higher coordination number during shearing, which would inhibit the rotation of bigger particles. Therefore, the smaller rotation of bigger particles is associated with a high coordination number. On the other hand, smaller particles have low coordination numbers, which permits relatively

easy rotation. Small particles play a role, like ball bearings in between big particles, which reduces the overall shear strength of the assembly. Table 1 shows the average rotations observed for small particles, big ones, and complete assembly.

4.2.5 Effect of confining pressure on the rotation

Biaxial tests with circular rods are conducted at three confining pressures σ_3 = 19.6, 39.2, and 58.8 kPa. The rotational behavior of circular assemblies is investigated under all three confining pressures to verify the effect of confining pressure. Interestingly, it is observed that the confining pressure has no significant impact on the rotational behavior of particles. Figure 16 shows the comparison of cumulative rotation distribution histograms (same as shown in Fig. 9) under different confining pressures. It can be seen that all three plots show very similar distribution patterns indicating that the overall rotational behavior of all particles is not much affected by confining pressure. Furthermore, rotations are symmetrically distributed around an average value of 0° in all cases.

Figure 17 shows the spatial distribution of cumulative particle rotations under three confining pressures. In all cases, significant rotations are exhibited by particles present in shear localization zones, i.e., along diagonals of the biaxial chamber. Furthermore, the rotation of particles on boundaries is observed in all cases. Usually, it can be seen that any rotation is accompanied by opposite rotating neighboring particles. Moreover, group of neighboring particles exhibiting rotations in same direction (rotation clusters) can also be observed in all cases. Overall similar rotational behavior is observed under different confining pressures, which confirms that rotational behavior in granular materials is not affected by the magnitude of confining pressure. Table 2 shows the mean clockwise, counterclockwise, and absolute rotations for three confining pressures.

5 Conclusions

Particle rotation of dual-sized circular assemblies is measured during the biaxial shearing test under three different confining pressures. When circular assemblies are subjected to deformations under loadings, particles displace and rotate. The magnitude of displacement and rotation of each particle depends on its location in the assembly and size.

Due to rigid boundary conditions and strain-controlled shearing, the particle displacements were governed by boundary movements in such a way that the particles present on top of the assembly moved downward initially. Later, the trajectories diverted outward (toward side walls) due to lateral expansion during shearing. The bottom wall is fixed, so particles undergo very small displacement close to the bottom wall. Unlike displacement patterns, the particles are free to exhibit any rotation. In all cases at around 20% deviatoric strain, more than 56% of particles show significant rotations, i.e., greater than 10°. Around 49.5% of particles exhibit clockwise, and 50.5% exhibit counterclockwise rotations of almost identical magnitudes, and the average particle rotation was zero. Rotation in both directions (clockwise and counterclockwise) increases simultaneously with the major principal strain confirming zero average rotation within the system at all instants. The particles exhibit rapid rotations at the beginning stage of the shearing, and as the deformations progress, the rotation growth becomes moderate. Rapid rotations at the start of the test indicate that as the deformation starts, the particles try to stable themselves, and in doing that, they may exhibit rotations. Big particles, due to high coordination number tend to rotate lesser and hence proved to be more resistant to rotations. Smaller particles due to low coordination number rotate more and act like ball bearings between big particles, which may reduce the overall shear strengths of the assembly. The absolute average cumulative rotations calculated at the end of shearing for σ_3 = 19.6, 39.2, and 58.8 kPa are 18.56°, 18.59°, and 18.54°, respectively, verifying that confining pressure has no significant influence on rotational behavior. Particles present in the shear band rotate more than particles present outside. Absolute average cumulative rotation outside the shear band increases from 0.1 to 4% major principal strain and becomes almost constant while the rotations inside the shear band rise immediately after the shearing starts and keep increasing throughout the test. Thanks to the accurate measurements of particle kinematics, it was possible to measure particle connectivity, i.e., coordination number. The results showed that the average particle connectivity decreases during shearing and ultimately bands of particles with low coordination numbers associated with higher rotations develop. Kinematic analyses show that these regions correspond to macroscopic shear bands.

Acknowledgments Ministry of Education, Culture, Sports, Science, and Technology of Japan is acknowledged for providing financial assistance through the Monbukagakusho scholarship to the first author to study at Yokohama National University, Japan. This work was funded by JSPS KAKENHI under grants 24360192 and 19H00780 to the corresponding author. In addition, support from the Royal Society IES/R1/201238 International Exchanges grant for the 4th and 2nd authors is also acknowledged. We thank the editor and anonymous reviewers for their insightful comments and suggestions.

Funding Open access funding provided by Yokohama National University.

Data availability The datasets generated during and analyzed during the study are available from the corresponding author upon reasonable request.

Declarations

Conflict of interest The authors have no competing interests to declare relevant to this article's content.

References

1. Andò E, Hall SA, Viggiani G, Desrues J, Bésuelle P (2012) Grain-scale experimental investigation of localised deformation in sand: a discrete particle tracking approach. Acta Geotech 7(1):1–13. https://doi.org/10.1007/s11440-011-0151-6
2. Bardet JP (1994) Observations on the effects of particle rotations on the failure of idealized granular materials. Mech Mater 18(2):159–182. https://doi.org/10.1016/0167-6636(94)00006-9
3. Bardet JP, Proubet J (1991) A numerical investigation of the structure of persistent shear bands in granular media. Geotechnique 41(4):599–613. https://doi.org/10.1680/geot.1991.41.4.599
4. Calvetti F, Combe G, Lanier J (1997) Experimental micromechanical analysis of a 2D granular material: relation between structure evolution and loading path. Mech Cohesive-Frict Mater 2(2):121–163. https://doi.org/10.1002/(SICI)1099-1484(199704)2:2%3c121::AID-CFM27%3e3.0.CO;2-2
5. Catalano E, Chareyre B, Barthélémy E (2014) Pore-scale modeling of fluid-particles interaction and emerging poromechanical effects. Int J Numer Anal Methods Geomech 38(1):51–71. https://doi.org/10.1002/nag.2198
6. Chen Z, Omidvar M, Li K, Iskander M (2017) Particle rotation of granular materials in plane strain. Int J Phys Model Geotech 17(1):23–40. https://doi.org/10.1680/jphmg.15.00046
7. Cho G-C, Dodds J, Santamarina JC (2006) Particle shape effects on packing density, stiffness and strength—natural and crushed sands. J Geotech Geoenviron Eng 5(132):591–602
8. Ciantia MO, Arroyo M, O'Sullivan C, Gens A, Liu T (2019) Grading evolution and critical state in a discrete numerical model of Fontainebleau sand. Geotechnique 69(1):1–15. https://doi.org/10.1680/jgeot.17.P.023
9. Crocker JC, Grier DG (1996) Methods of digital video microscopy for colloidal studies. J Colloid Interface Sci 179(1):298–310. https://doi.org/10.1006/jcis.1996.0217
10. Cundall PA (1979) A discrete numerical model for granular assemblies. Geeotechnique 29(29):47–65. https://doi.org/10.1680/geot.1979.29.1.47
11. Hall SA, Bornert M, Desrues J, Pannier Y, Lenoir N, Viggiani G, BéSuelle P (2010) Discrete and continuum analysis of localised deformation in sand using X-ray μCT and volumetric digital image correlation. Geotechnique 60(5):315–322. https://doi.org/10.1680/geot.2010.60.5.315
12. Horne MR (1965) The behaviour of an assembly of rotund, rigid, cohesionless particles. II. Proc R Soc Lond Ser A Math Phys Sci 286(1404):79–97. https://doi.org/10.1098/rspa.1965.0131
13. Huang J, da Silva MV, Krabbenhoft K (2013) Three-dimensional granular contact dynamics with rolling resistance. Comput Geotech 49:289–298. https://doi.org/10.1016/j.compgeo.2012.08.007
14. Iwashita K, Oda M (1998) Rolling resistance at contacts in simulation of shear band. J Eng Mech 124(March):285–292
15. Kuhn MR (1999) Structured deformation in granular materials. Mech Mater 31(6):407–429. https://doi.org/10.1016/S0167-6636(99)00010-1
16. Kuhn MR, Bagi K (2002) Particle rotations in granular materials. 15th ASCE Eng Mech Conf 6(June):2002
17. Lenoir N, Bornert M, Desrues J, Bésuelle P, Viggiani G (2007) Volumetric digital image correlation applied to x-ray microtomography images from triaxial compression tests on argillaceous rock. Strain 43(3):193–205. https://doi.org/10.1111/j.1475-1305.2007.00348.x
18. Mahmood Z, Iwashita K (2009) Influence of particle shape on shear band formation of quasi-static granular media. J Appl Mech 12(August):481–488. https://doi.org/10.1007/978-3-540-77074-9_54
19. Misra A, Jiang H (1997) Measured kinematic fields in the biaxial shear of granular materials. Comput Geotech 20(3–4):267–285. https://doi.org/10.1016/s0266-352x(97)00006-2
20. Nitka M, Grabowski A (2021) Shear band evolution phenomena in direct shear test modelled with DEM. Powder Technol 391:369–384. https://doi.org/10.1016/j.powtec.2021.06.025
21. O'Sullivan C (2011) Particulate discrete element modelling a geomechanics perspective, 1st edn. Spon Press, London
22. Oda M (1972) The mechanism of fabric changes during compressional deformation of sand. Soils Found 12(2):1–18
23. Oda M, Konishi J, Nemat-Nasser S (1982) Experimental micromechanical evaluation of strength of granular materials: effects of particle rolling. Mech Mater 1:269–283
24. Omidvar M, Chen ZC, Iskander M (2015) Image-based lagrangian analysis of granular kinematics. J Comput Civ Eng 29(6):04014101. https://doi.org/10.1061/(asce)cp.1943-5487.0000433
25. Rorato R, Arroyo M, Gens A, Andò E, Viggiani G (2021) Image-based calibration of rolling resistance in discrete element models of sand. Comput Geotech. https://doi.org/10.1016/j.compgeo.2020.103929
26. Rorato R, deToledo MAA, Andò ECG, Gens A, Viggiani G (2020) Linking shape and rotation of grains during triaxial compression of sand. Granul Matter 22(4):1–21. https://doi.org/10.1007/s10035-020-01058-2
27. Rowe PW (1962) The stress-dilatancy relation for static equilibrium of an assembly of particles in contact. Proc R Soc Lond Ser A Math Phys Sci 269(1339):500–527. https://doi.org/10.1098/rspa.1962.0193
28. Schneebeli M (1956) Mechanique des soils-Une analogie mechanique pour les terres sans cohesion. Comptes Rendes Hebdomaires Des Seances l'Academie Des Sci 243:125–126
29. Shahin HM, Sung E, Nakai T, Hinokio M, Kikumoto M, Yamamoto M, Tabata Y (2006) 2D model tests and numerical simulation in shallow tunneling considering existing building load. Undergr Constr Ground Mov 155:304–311. https://doi.org/10.1061/40867(199)37
30. Šmilauer V, Catalano E, Chareyre B, Dorofeenko S, Jakob C (2015) Yade documentation. 526, https://doi.org/10.5281/zenodo.34073
31. Tong ZX, Zhang LW, Zhou M (2013) DEM simulation of biaxial compression experiments of inherently anisotropic granular

materials and the boundary effects. J Appl Math. https://doi.org/10.1155/2013/394372
32. Wen Y, Zhang Y (2021) Evidence of a unique critical fabric surface for granular soils. Geotechnique. https://doi.org/10.1680/jgeot.21.00126
33. Yimsiri S, Soga K (2010) Dem analysis of soil fabric effects on behaviour of sand. Geotechnique 60(6):483–495. https://doi.org/10.1680/geot.2010.60.6.483